INSTITUTE OF PHYSICS PUBLISHING PLASMA PHYSICS AND CONTROLLED FUSION

Plasma Phys. Control. Fusion **44** (2002) 611–625 PII: S0741-3335(02)32247-4

Transport in island divertors: physics, 3D modelling and comparison to first experiments on W7-AS*

Y Feng[1], F Sardei[1], P Grigull[1], K McCormick[1], J Kisslinger[1], D Reiter[2] and Y Igitkhanov[1]

[1] Max-Planck-Institut für Plasmaphysik, IPP-EURATOM-Association, D-85748 Garching, Germany
[2] Institut für Plasmaphysik, Forschungszentrum Jülich Gmbh, EURATOM Association, Trilateral Euregio Cluster, D-52425 Jülich, Germany

Received 3 January 2002, in final form 20 March 2002
Published 30 April 2002
Online at stacks.iop.org/PPCF/44/611

Abstract

Basic plasma transport properties in island divertors are compared to those of standard tokamak divertors. A realistic plasma transport modelling of high-density discharges in island divertors has become possible by implementing a self-consistent treatment of impurity transport in the EMC3-EIRENE code. In contrast to standard tokamak divertors, the code predicts no high recycling prior to detachment, with the downstream density never exceeding the upstream density. This is mainly due to momentum losses arising from the cross-field transport associated with the specific island divertor geometry. This momentum loss is effective already at low densities, high temperatures and is responsible for the high upstream densities needed to achieve detachment. Numerical scans of carbon concentration for high-density plasma typically show first a smooth, then a sharp increase of the carbon radiation, the latter being accompanied by a sharp drop of the downstream temperature and density indicating detachment transition. The jumps of the radiation and temperature are due to a thermal instability associated with the form of the impurity cooling rate function and can be reproduced by a simple 1D radial energy model based on cross-field transport and impurity losses. This model is used as a guideline to illustrate and discuss the detachment physics in details, including detachment condition and thermal instability. Major EMC3-EIRENE code predictions have been verified by the first W7-AS divertor experiments. A comparison of calculations and measurements is presented for high-density, high-power W7-AS divertor discharges and the physics related to rollover and detachment is discussed in detail. The code has been recently extended to general SOL configurations with open islands and arbitrary ergodicity by using a new highly accurate field-line mapping technique. The method correctly reproduces flux surfaces and islands over a high number of toroidal field periods, thus ensuring a clear distinction between parallel and radial transport. The technique has been tested

* This paper is an extension of work originally presented at the 28th EPS Conf., Madeira.

successfully on W7-AS, W7-X, LHD and TEXTOR DED, and first applied to solve the coupled heat conduction equations for a typical ergodic W7-AS configuration.

1. Introduction

Basic features of the island divertor concept have been investigated theoretically and experimentally in the past few years [1–5]. A realistic plasma transport modelling for these configurations has become possible with the EMC3-EIRENE code [6, 7], which was developed in close interaction with the W7-AS experiment and was already applied to pre-divertor experimental studies with island divertor configurations [4, 8]. Recently the code has been extended to include impurity transport, which now allows a self-consistent treatment of plasma, neutrals and impurities in a realistic geometry taking into account the complex 3D island structures and the discontinuous divertor plates and baffles [9].

After reviewing the basic differences between the island divertor for low-shear stellarators and the standard tokamak divertor (section 2), this paper presents a numerical study with the EMC3-EIRENE code on plasma and impurity transport and on detachment in the W7-AS island divertor in section 3. In section 4 the basic features of the detachment transition observed in the 3D model are illustrated on a simple 1D radial model, which is also used for an analytical derivation of the underlying physics. Section 5 compares the 3D modelling to the first experimental results on W7-AS. Section 6 presents first applications of a new 3D mapping technique which represents a substantial extension of the EMC3-EIRENE code by enabling it to model arbitrary edge configurations, including open island structures and stochastic fields.

2. Island divertor versus standard tokamak divertors

Although the plasma boundaries of island divertors and tokamak poloidal-field divertors are governed by the same physics, leading geometrical parameters are significantly different, which is reflected in different weights of the transport and recycling processes. For example, the field-line pitch in the islands, $\Delta\iota r/R$, with $\Delta\iota \approx \iota' r_\mathrm{i}$ being the variation of the rotational transform over r_i, the island width, is about two orders of magnitude smaller than that of tokamak divertors, $\iota r/R \approx 0.1$. This parameter measures the poloidal progression of a field line in the island reference frame and scales as $1/L_\mathrm{c}$, where L_c is half the target-to-target connection length at the power carrying channel in the island SOL. The small pitch is mainly due to the small value of $\Delta\iota \propto \sqrt{\iota'\hat{B}}$, which results both from the weak diverting field in island divertors compared to tokamak divertors, $\hat{B} \equiv \Delta B/B < 10^{-3}$ and, for W7-AS and W7-X, from low shear. (The $\Delta\iota$ scaling results from $r_\mathrm{i} \propto \sqrt{\hat{B}/\iota'}$ [10].) The small pitch explains why L_c for island divertors ($\approx$100 m for W7-AS and W7-X) is generally larger than L_c for even large tokamaks. The distance between the main plasma and the target plates is also much smaller than in tokamaks, leading to a less efficient screening of the recycling neutrals from the bulk plasma. Both a larger L_c and a smaller plasma-to-target distance increase the role of cross-field transport. A further difference is the inherent three-dimensionality of island divertors. It arises from the discontinuity of the target and baffle plates, which defines periodically localized recycling zones along the islands, and from the toroidal variation of the radial island width, which causes inhomogeneous radial transport fluxes. Both effects lead, for low temperatures,

to a periodic modulation of the plasma parameters along the islands, which cannot be smoothed out by parallel heat conduction [2].

The prominent role of the cross-field transport in the W7-AS island divertor was already demonstrated by previous EMC3-EIRENE simulations without impurities for high-density plasmas prior to detachment [4] and is discussed in this paper for detachment conditions (section 4). Compared to tokamaks, the downstream density n_{ed} typically shows a roughly linear scaling with the upstream density n_{eu} indicating no high recycling and never exceeding n_{eu}. The downstream temperature T_{ed} decreases with n_{eu} faster than $T_{ed} \propto n_{eu}^{-2/3}$ (linear regime) but slower than $T_{ed} \propto n_{eu}^{-2}$ (high recycling tokamak regime). The upstream temperature T_{eu} drops significantly with n_{eu} even in the case of $T_{ed} \ll T_{eu}$. The ratio of the downstream and upstream total pressures $2n_{ed}T_{ed}/n_{eu}T_{eu}$ is clearly below unity even at low densities, high temperatures, indicating a significant momentum loss of the plasma ions flowing in the main channel.

3. 3D modelling

3.1. Impurity model

The study presented in this paper required a self-consistent modelling of the impurity transport and radiation in the island SOL. To this aim the following impurity model was implemented in the EMC3-EIRENE code:

continuity:

$$\nabla \cdot (n_I V_{I\|} \boldsymbol{b} - D_I \boldsymbol{b}_\perp \boldsymbol{b}_\perp \cdot \nabla n_I) = -S_{z\to z+1} - R_{z\to z-1} + S_{z-1\to z} + R_{z+1\to z}; \quad (1)$$

momentum (force balance):

$$U_{Ii}(V_{I\|} - V_{i\|}) = -\boldsymbol{b} \cdot \nabla n_I T_I + n_I e Z_I E_\| + n_I Z_I^2 C_e \boldsymbol{b} \cdot \nabla T_e + n_I C_i \boldsymbol{b} \cdot \nabla T_i \quad (2)$$

$$n_e e E_\| + \boldsymbol{b} \cdot \nabla n_e T_e + n_e C_e \boldsymbol{b} \cdot \nabla T_e = 0, \quad (3)$$

with $T_I = T_i$. The model applies to light impurities at small concentrations, $Z_I^2 n_I \ll n_e$, which means that the impurities affect the plasma only via radiation losses. High density and low temperature are assumed in the momentum equation (2), which implies that impurity inertial and viscous forces are negligible compared to friction forces with the main plasma flow. In this study carbon released from the target by sputtering processes is assumed to be the only impurity species, the concentration being controlled by the total sputtering coefficient, S_c, which is used as a free parameter.

3.2. W7-AS model configuration

The boundary of the standard W7-AS divertor configuration consists of a chain of macroscopic islands originating from resonant intrinsic field perturbations at the edge rotational transform $\iota_a = 5/9$ (figure 1(*c*)). All magnetic and plasma-facing structures exhibit the basic five-fold toroidal periodicity and up/down symmetry of the device. Figure 1(*c*) shows a cross section of the 3D plasma computational domain used in the EMC3-EIRENE code including the nine islands and the target plate and baffles at the position of the bottom divertor. The grid extends smoothly inwards into the core and outwards into the magnetic structures facing the wall, as shown in the figure.

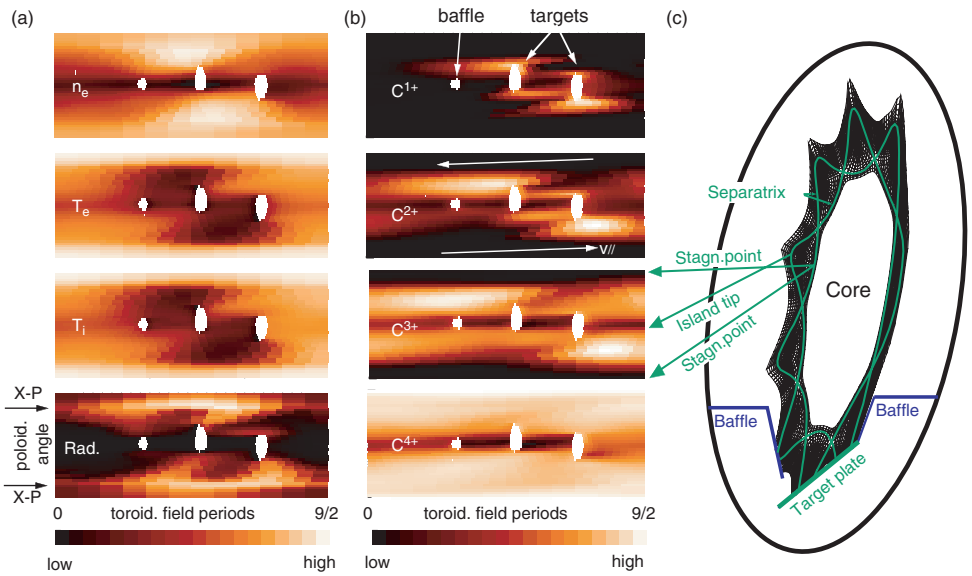

Figure 1. (*a*) Plasma parameters and (*b*) lower ionization state of carbon along an island tube intersecting the targets: (*a*) $S_c = 1.5$ (detached case), (*b*) $S_c = 0.5$ (attached case). Parameters range in the pictures (logarithmic scale): $n_e \approx 2 \times 10^{18}$–$2 \times 10^{20}\,\mathrm{m}^{-3}$, $T_e \approx T_i \approx 0.5$–$20\,\mathrm{eV}$, Rad. ≈ 0.2–$10\,\mathrm{W\,cm}^{-3}\,\mathrm{s}^{-1}$, $C^{i+} \approx 10^{16}$–$10^{18}\,\mathrm{m}^{-3}$. (*c*) W7-AS island configuration as used in the EMC3-EIRENE code.

3.3. Modelling results

An example of how the discontinuous target plates typically affect the distribution of the plasma parameters, carbon radiation and first four ionization states of carbon over an island tube cut by the plates and baffles are shown in figure 1. The power entering the SOL is $P_{SOL} = 1\,\mathrm{MW}$, the upstream electron density at the separatrix $n_{eu} = 8 \times 10^{19}\,\mathrm{m}^{-3}$. In the recycling region, which is defined by the position of the discontinuous targets, the plasma density has a maximum and the temperature a minimum, as expected (figure 1(*a*)). Toroidally away from this region, a temperature gradient arises (T modulation by a factor of $\approx$3) in order to sustain the parallel heat conduction to the recycling region (figure 1(*a*)). The plasma density exhibits the opposite gradient according to constant plasma pressure. For the sputtering coefficient used in this calculations, $S_c = 1.5$, the radiation zone is detached from the targets and peaks at the X-points (figure 1(*a*)). The ionization distribution over the island tube (figure 1(*b*)) is best visualized by using a small sputtering coefficient, $S_c = 0.5$, which keeps the radiation zone attached to the plates at $T_e \approx 8\,\mathrm{eV}$. The first ionization state is strongly localized near the plates due to its short life time. Higher states live longer, spread in toroidal and poloidal direction and are shifted downstream by friction with the main plasma flow. C^{4+} is homogeneous everywhere except in the shadowed regions between the plates, and higher ionization states are not present at the given SOL temperatures.

The detachment physics in the W7-AS island divertor was explored in a dedicated numerical transport study with the EMC3-EIRENE code including intrinsic carbon impurities. The carbon sputtering coefficient S_c was varied from 0.5% to 5% (figure 2). A total power of 1 MW entering the island SOL was kept fixed in all simulations, the transport coefficients were $D = 0.5\,\mathrm{m}^2\,\mathrm{s}^{-1}$ for both hydrogen and carbon, and $\chi_e = \chi_i = 3D$. These estimates for D and χ_e were taken from the results of a comparison between simulated and measured

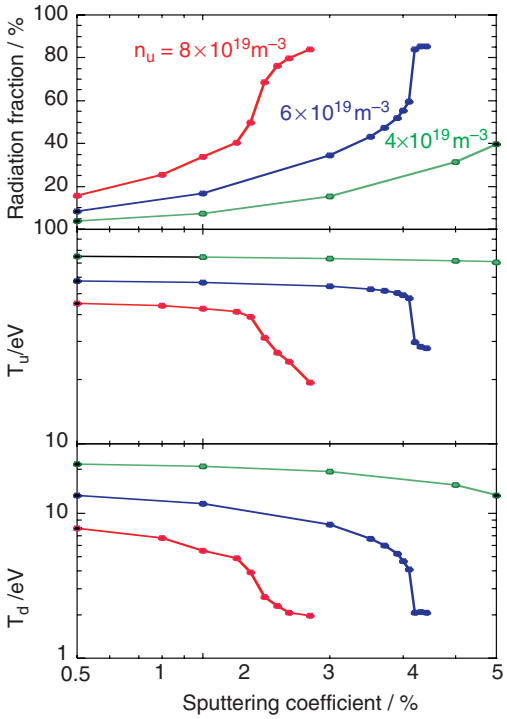

Figure 2. Sharp increase of radiation and drop of T at detachment transition.

radial density profiles in the shadowed region between the discontinuous targets and power flux profiles on the target plates, respectively [11]. Three upstream electron density values were used: $n_{eu} = 4 \times 10^{19}$, 6×10^{19} and $8 \times 0^{19}\,m^{-3}$. In the lowest density case, the carbon radiation increases smoothly from 5% to 40%, reflecting essentially the linear scaling of the radiation with the impurity density. The up- and downstream temperatures are almost insensitive to S_c, indicating a weak impact of the radiation on the power balance in the SOL. For the intermediate density, $n_{eu} = 6 \times 10^{19}\,m^{-3}$, the carbon radiation first increases smoothly with S_c up to 3.1% and then jumps to a high radiation level at which the carbon radiates more than 80% of the SOL input power. The jump is accompanied by a sharp drop of both the up- and downstream temperatures. A concomitant drop of the pressure and recycling flux (not shown in the picture) indicates detachment. If n_{eu} is increased to $8 \times 10^{19}\,m^{-3}$, the value of S_c needed for detachment is shifted down to 1.5% and the detachment transition becomes smoother. In all cases the contribution from hydrogen radiation to the power balance stays below 10%. The radiation zone is thin compared to the island size and jumps from the target to the X-point at detachment transition, $S_c = 1.3$–1.5% (figure 3, high-density case). The target power load drops strongly at detachment and hot spots disappear, indicating a broad deposition profile.

4. Physics of detachment

4.1. 1D model

In order to identify the basic physical mechanisms underlying the effects shown in figures 2 and 3 and to clarify the role of the cross-field transport in the detachment process, the energy

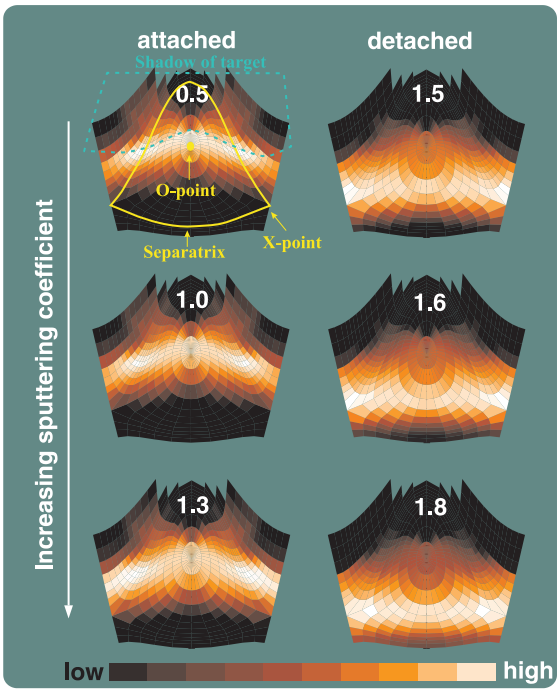

Figure 3. Distribution of carbon radiation averaged along an island tube. The radiation zone jumps from the target to the X-point at detachment transition (sputtering coefficient between 1.3 and 1.5).

transport was modelled by the 1D plasma 'radial' heat balance equation with impurity radiation loss term:

$$\frac{\mathrm{d}q}{\mathrm{d}x} = -Cn^2L(T) \tag{4}$$

with

$$q = -D_{\mathrm{eff}}\frac{\mathrm{d}T}{\mathrm{d}x}, \tag{5}$$

where x is the radial direction defined in figure 4(a), C the impurity concentration and $L(T)$ the cooling rate for carbon shown in figure 4(b). The radial components of the heat conductivity are $D_{\mathrm{eff}} = \chi n$ and $D_{\mathrm{eff}} = \chi n + \Theta^2\kappa T^{5/2}$ for the SOL zones (A) and (B) in figure 4(a) bounded by the inner and outer separatrix, respectively. $\Theta = \Delta tr/R = 0.001$ is the pitch angle. Boundary conditions are given by the heat fluxes at the upstream position (separatrix) and downstream position (target):

$$q_{\mathrm{u}} = \frac{P_{\mathrm{SOL}}}{4\pi^2 Ra}, \tag{6}$$

$$q_{\mathrm{d}} = \Theta nc_{\mathrm{s}}(\gamma T_{\mathrm{d}} + 31\,\mathrm{eV}), \tag{7}$$

where P_{SOL} is power entering the SOL and c_{s} the sound speed. The solution of this 1D problem is shown in figures 5(a) and (b) for $P_{\mathrm{SOL}} = 1\,\mathrm{MW}$, $n = 8\times10^{19}\,\mathrm{m}^{-3}$, $\chi = \chi_{\mathrm{e}} + \chi_{\mathrm{i}} = 3\,\mathrm{m}^2\,\mathrm{s}^{-1}$. It reproduces two basic features of the detachment transition already found in the 3D EMC3-EIRENE simulations, namely the sharp increase of the radiation and the jump of the radiation front from the target to the separatrix at detachment transition (figures 2 and 3).

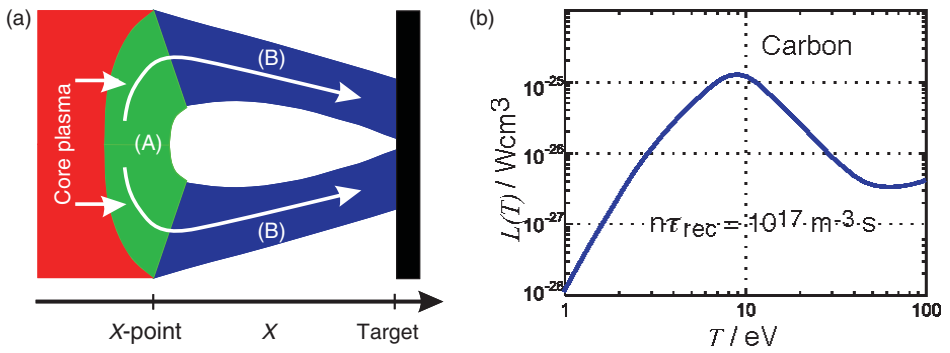

Figure 4. (*a*) SOL geometry for the 1D: 'radial' energy model. (*b*) Cooling rate for carbon [12].

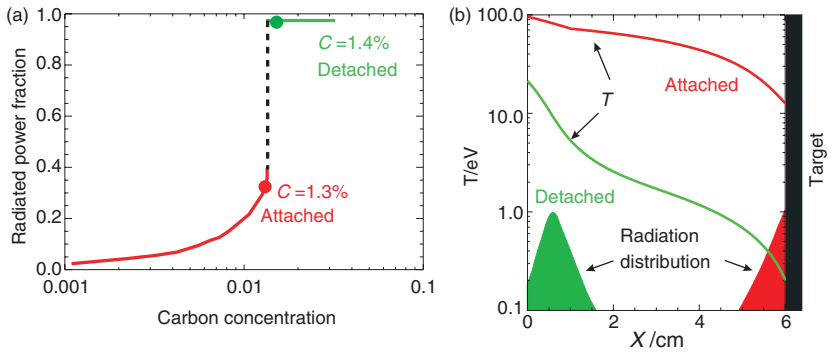

Figure 5. (*a*) Jump of the radiation level at carbon concentration between 1.3% and 1.4%. No stable solutions in the radiation range between 40% and 95%. (*b*) Jump of the radiation zone from target to separatrix at detachment transition.

The contribution of the parallel transport to the mentioned effects is negligible since the parallel heat conductivity accounts less than 2% of the total conductivity D_{eff} for the given parameters and the relevant temperature of about 10 eV for carbon. That is, the consistency of the results from the 1D and 3D models identifies the cross-field transport and the impurity radiation as being the basic ingredients of the detachment physics in the W7-AS island divertor.

The physics related to the jump of the radiation zone (figure 5(*b*)) and the radiation level (figure 5(*a*)) at detachment transition will be elucidated in the following two sections, respectively.

4.2. Detachment condition

The same 1D model, equations (4) and (5), can be used to derive a detachment condition for island divertors. For any given radial profile of T and $C\chi n^3$, equation (4) may be integrated from the separatrix to the target after multiplying with equation (5) and switching from the x to the T variable:

$$q_{\text{u}}^2 - q_{\text{d}}^2 = \int_{T_{\text{d}}}^{T_{\text{u}}} 2C\chi n^3 L(T)\,\mathrm{d}T \tag{8}$$

with $D_{\text{eff}} = \chi n$ and q_{u} and q_{d} from equations (6) and (7). In a detached state $T_{\text{d}} \to 0$ and $q_{\text{d}} \to 0$. The radial extension of the radiation layer can be estimated from the heat conduction

equation $q_u = -\chi n T_{rad}/\lambda$ with T_{rad} the relevant impurity radiation temperature and λ the layer thickness. We get $\lambda = 0.5$–1 cm, which is small compared to the thickness of the island SOL ($\approx$5 cm). By assuming a peaked cooling rate function (figure 4(*b*)) and a smooth radial profile of $C\chi n^3$, both in agreement with 3D results, equation (8) can be approximated by

$$q_u = \underbrace{\sqrt{\int_0^\infty L(T)\,\mathrm{d}T}}_{\text{const}} \sqrt{(2C\chi n^3)_{x_{rad}}}, \tag{9}$$

with $\text{const}\sqrt{(2C\chi n^3)_{x_{rad}}}$ the radiation capability at x_{rad}, the location of the radiation layer. Detachment occurs if the radiation capability at the target equals or exceeds the input power:

$$\text{const}\sqrt{(2C\chi n^3)_{x_{target}}} \geqslant q_u. \tag{10}$$

The detachment is stable within the SOL if the radiation capability is higher than the input power at the target and lower at the separatrix:

$$\text{const}\sqrt{(2C\chi n^3)_{x_{target}}} > q_u > \text{const}\sqrt{(2C\chi n^3)_{x_u}}. \tag{11}$$

In agreement with this model, stable detachment within the SOL was not found in the 3D simulations for the given input parameters, as evidenced by the jump of the radiation from the target to the separatrix at detachment transition (figure 3). This is consistent with the smooth distributions of n and C resulting from a strong cross-field transport and with the assumed constant χ value.

4.3. Bifurcation and thermal instability

Let us now look closer to the physics of the detachment transition. A refined numerical S_c scan with EMC3-EIRENE in the range of detachment transition shows that the forward and backward transitions occur at different values of S_c giving rise to a hysteresis loop (figure 6(*a*)). This effect is related to the two-branch shape of the cooling rate function $L(T)$ (figure 6(*c*)) and becomes clear by inspecting the radial power balance, equation (8), with $C\chi n^3$ taken at the target and T_u replaced by ∞:

$$q_u^2 = (2C\chi n^3)_{x_{target}} \int_{T_d}^\infty L(T)\,\mathrm{d}T + q_d^2 \tag{12}$$

with q_d given by equation (7). This equation has three solutions for $T_d(C)$ within a small range of impurity concentrations C, namely two stable branches, corresponding to the high- and low-T legs of $L(T)$, respectively, and an unstable intermediate branch connecting the two (figure 6(*b*)). The three branches can be easily identified by taking the derivative of T_d with respect to C from equation (12) for a fixed input power q_u:

$$\frac{\partial T_d}{\partial C} = \frac{(1/C)\int_{T_d}^\infty L(T)\,\mathrm{d}T}{L(T_d) - F(T_d)} \tag{13}$$

with

$$F(T_d) = \frac{3\gamma T_d + 31\,\text{eV}}{\gamma T_d + 31\,\text{eV}} \frac{1}{(2C\chi n^3)_{x_{target}} T_d} q_d^2 \tag{14}$$

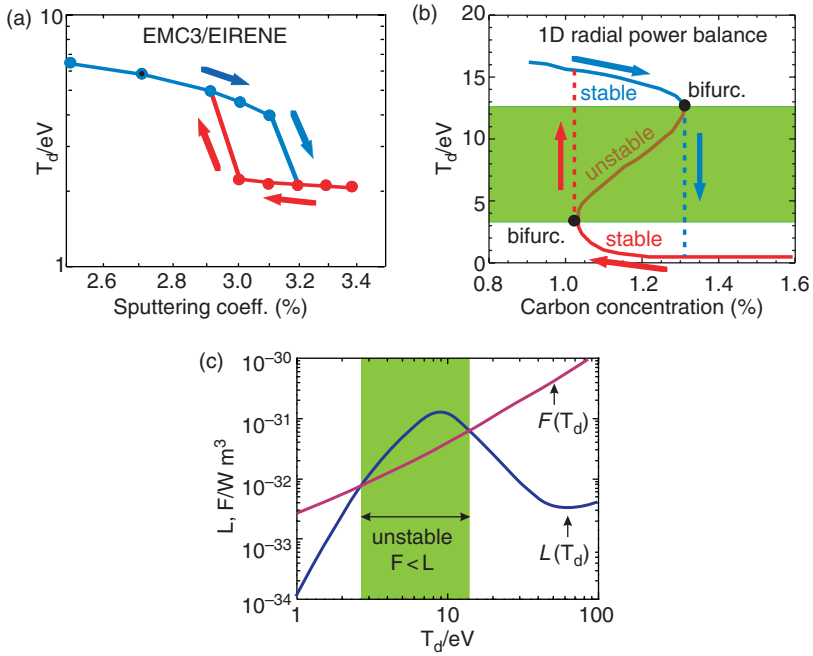

Figure 6. Two-branch transition (hysteresis loop) between attached and detached state: (*a*) EMC3-EIRENE simulations; (*b*) 1D radial power balance; (*c*) cooling rate for carbon and function $F(T_\mathrm{d})$ from equation (14).

The three branches are defined by the sign of $\partial T_\mathrm{d}/\partial C$, i.e. by the relative magnitude of $L(T_\mathrm{d})$ and $F(T_\mathrm{d})$:

$$\begin{aligned} F(T_\mathrm{d}) > L(T_\mathrm{d}) &\Rightarrow \frac{\partial T_\mathrm{d}}{\partial C} < 0 \qquad \text{(stable high-}T_\mathrm{d}\text{ and low-}T_\mathrm{d}\text{ solutions)},\\ F(T_\mathrm{d}) = L(T_\mathrm{d}) &\Rightarrow \frac{\partial T_\mathrm{d}}{\partial C} = \infty \qquad \text{(bifurcation)},\\ F(T_\mathrm{d}) < L(T_\mathrm{d}) &\Rightarrow \frac{\partial T_\mathrm{d}}{\partial C} > 0 \qquad \text{(unstable solution)}. \end{aligned} \tag{15}$$

The unstable branch is not accessible. If C is increased beyond the high-T_d bifurcation point, the plasma enters the unstable T_d domain and relaxes dynamically into the stable low-T_d solution. The reverse transition occurs if C is decreased beyond the low-T_d bifurcation point. For a given input power into the SOL, q_u, and for any given T_d we get, from equation (14), upon substitution of $(2C\chi n^3)_{x_\mathrm{target}}$ from equation (12):

$$F \propto \frac{q_\mathrm{d}^2}{q_\mathrm{u}^2 - q_\mathrm{d}^2} \propto \frac{n^2}{1 - (\mathrm{const}\cdot n)^2}. \tag{16}$$

That is, by increasing n, F shifts to higher values, whereby the unstable T_d domain, defined by the two intersections between $L(T)$ and $F(T)$ (figure 6(*c*)), and the hysteresis loop shrink and eventually disappear. This explains why the transition to detachment becomes smoother at the highest density case shown in figure 2.

5. Comparison to first experimental results

At present, the EMC3-EIRENE code uses a model configuration with closed magnetic islands (figure 1(c)). The size of these islands is about 30% smaller than that of the real W7-AS divertor configuration. This difference in island size may, to a certain extent, affect the details of the island transport, but should not influence the main physics issues addressed in this paper, as long as the cross-field transport dominates.

In order to allow a direct comparison of the predictions shown in figure 2 to the first experimental results, the calculations have been extended to a full upstream-density scan in the range (1–6) $\times 10^{19}\,\mathrm{m}^{-3}$. The power into the SOL, P_{SOL}, has been gradually reduced from 1 to 0.85 MW with increasing density up to detachment to account for increasing main plasma radiation at higher densities. The transport coefficients are the same as in the predictions shown in figure 2, the sputtering coefficient is kept fixed at 3%. Figure 7 shows a comparison of the predicted and measured [13] downstream electron density and normalized momentum loss versus upstream density, $n_{\mathrm{es}}(\equiv n_{\mathrm{eu}})$. The roughly linear relation between n_{ed} and n_{es} found in the code simulations even at high upstream densities (figure 7, top) is verified by the experiment and confirms the previous predictions without impurities [4]. Density rollover is found at $n_{\mathrm{es}} = (5\text{–}6) \times 10^{19}\,\mathrm{m}^{-3}$, in agreement with the experiment. The reason for the absence of a high-recycling regime prior to detachment is the momentum loss arising from the cross-field transport associated with the specific island divertor geometry. This momentum loss is effective already at low densities, high temperatures, as shown by both the simulations and the experiments (figure 7, bottom) and is responsible for the high upstream densities needed to achieve detachment.

After the start of the divertor experiment, a detailed numerical study has been carried out with the input data n_{es} and P_{SOL} taken from the experiment and the measured $\bar{n}_{\mathrm{e}}$ as independent parameter. Figure 8 shows n_{es} and P_{SOL} versus $\bar{n}_{\mathrm{e}}$ as estimated from the experiment [13] (left) and as used in the code (right). In the meantime, the experimental $n_{\mathrm{es}}(\bar{n}_{\mathrm{e}})$ data set prior to

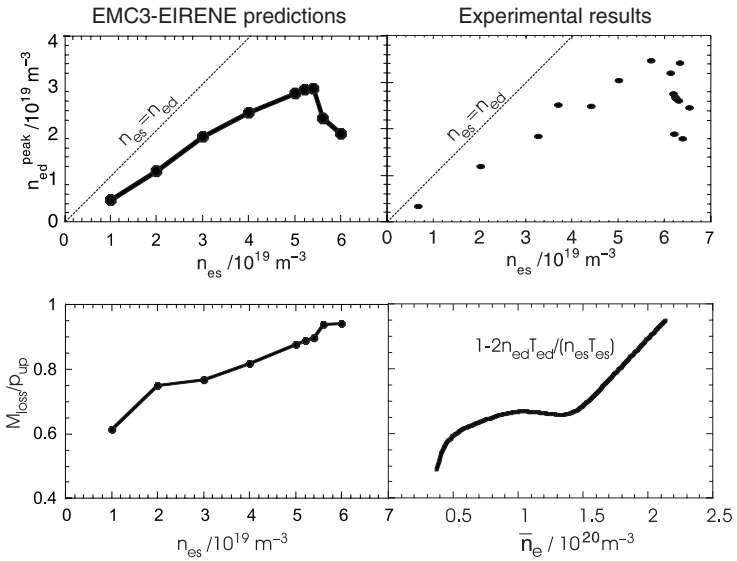

Figure 7. Absence of high recycling prior to detachment (top) and momentum loss at low densities (bottom).

rollover has been enlarged revealing a fine structure not yet discussed in [13] (see normal-to-improved-confinement transition [14, 15]). These additional data are not shown here as they do not affect any aspect of the SOL transport analysis presented in this paper. At high $\bar{n}_e$ values, P_{SOL} strongly drops due to enhanced core impurity radiation. The calculated n_{ed} values (figure 9) reproduce correctly the measured upward/downward dependency on $\bar{n}_e$ including a rollover value of about $4 \times 10^{19}\,m^{-3}$ at $\bar{n}_e \approx (2\text{–}2.5) \times 10^{20}\,m^{-3}$. Here the calculated core ionization fraction, S_{core}, has a minimum (figure 9), which reflects the improved neutral screening at maximum n_{ed} (attached ionization front, $T_{ed} \approx 10\,eV$, not shown here). If $\bar{n}_e$ is increased further, P_{SOL} and T_{ed} continuously drop leading to a gradual inward shift of the ionization front, which in turn reduces n_{ed} (figure 9). At $\bar{n}_e \approx 2.8 \times 10^{20}\,m^{-3}$ the calculated n_{ed} drops sharply by 30% and S_{core} sharply rises from 4% to 14%, which indicates a jump of the ionization zone to the separatrix (detachment transition, $T_{ed} \approx 2\,eV$), in agreement with the detachment physics discussed in section 4.3. In the experiment, the n_{ed} density drop is even larger, which may be explained by a concomitant drop of the measured separatrix density, n_{es} (figure 8). A sharp increase of S_{core} during detachment transition means a stronger particle outflux through the separatrix, resulting in a larger $\bar{n}_e/n_{es}$ ratio. This is a possible explanation of the measured drop of n_{es} following a gradual, feedback-controlled increase of $\bar{n}_e$.

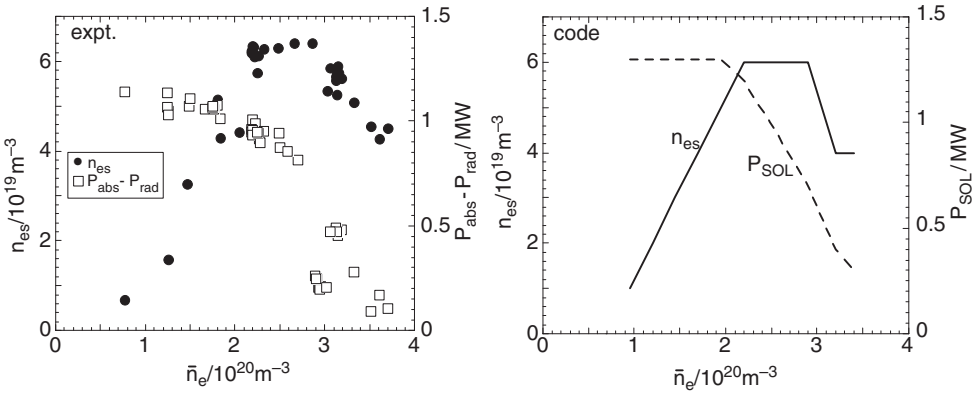

Figure 8. Separatrix densities and powers through the separatrix for high density 2 MW NBI-heated discharges. Left: experimental data set; right: corresponding EMC3-EIRENE input parameters.

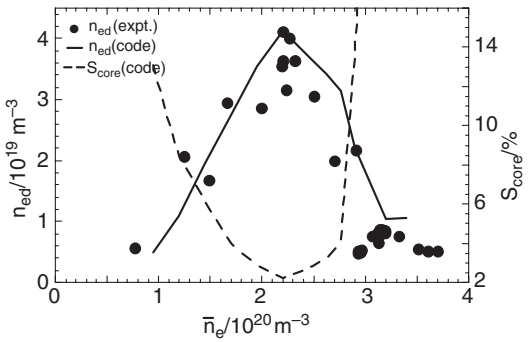

Figure 9. Downstream densities from experimental data and code calculations and simulated ionization fraction in the core. Dropping n_{ed} and rising S_{core} indicate shifting of the ionization front towards the separatrix and subsequent detachment.

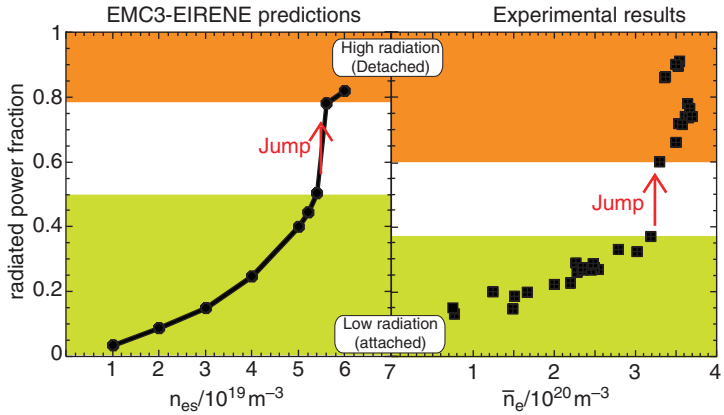

Figure 10. Jump of carbon radiation at detachment transition. n_{es} and $\bar{n}_e$ are the respective independent parameters for the code and the experiment.

Additionally, the EMC3-EIRENE code has predicted a jump of the carbon radiation at detachment transition (see figures 2 and 10). This effect has been derived in section 4.3 from the energy balance equation and is due to a thermal instability associated with the form of the impurity cooling rate function. Bolometric measurements for a large number of quasi-stationary discharges support this theory [16]. According to these first experimental results, the W7-AS island divertor can either be operated at a low radiation level (<40% of the absorbed power, attached case) or at a high radiation level (>60%, detached case), as shown in figure 10.

6. Extension of the EMC3-EIRENE code to arbitrary ergodicity

Although the W7-AS model configuration used up to now in the EMC3-EIRENE code is sufficiently accurate to describe the global physics effects in the island divertor, a local comparison is only possible by taking into account the full complexity of the magnetic structure, which is usually a combination of closed and open island sections and ergodic regions. For strongly ergodic boundaries, like those of LHD and TEXTOR-DED, approximations based on closed magnetic structures are, of course, not applicable.

These restrictions have been overcome recently by implementing a new 'reversible field-line mapping' (RFLM) technique in the EMC3 code, which avoids the crucial numerical diffusion of the parallel transport into the radial direction associated with standard numerical mapping methods. The mapping procedure is an efficient alternative to a standard numerical integration of a large number of field lines (e.g. GOURDON code), which is not affordable even for high-power parallel computers. The field lines are started from an arbitrary 2D grid defined in a poloidal cross section and covering the region of interest. They are traced with the GOURDON code over one field period and stored at given toroidal intervals. The RFLM technique addresses the transfer of a field line between the two cuts of the flux tubes merging at the same toroidal plane. The transfer of a field line is done by a two-step symmetric local interpolation on the overlapping areas of the two flux tubes facing each other at the cuts.

This procedure ensures a reversible mapping, i.e. the path of a field line after an arbitrary number of mapping steps is exactly recovered by backward mapping. In the examples presented in this paper, a linear interpolation is used for both steps. Several accuracy tests

have been carried out with the RFLM technique for W7-AS, W7-X, LHD and TEXTOR-DED configurations. They show that the radial deviation of the mapped field lines from 'exact' numeric integration (GOURDON code) for flux surfaces or islands, which is a crucial parameter for a correct numerical distinction between the parallel and the cross-field transport, remains bounded at very low level with increasing number of mapping steps (see 'mapping noise' in figure 11 for W7-AS). In other words, mapped field lines do not leave flux surfaces or islands for any relevant number of mapping steps, if the chosen grid is sufficiently fine. A comparison of the linear RFLM technique with the linear 'interpolated cell mapping' (ICM) technique [17] applied to W7-AS shows that the radial deviation of the same field line calculated with ICM exhibits a mapping noise of increasing amplitude drifting linearly away in the direction of increasing radius, with the drift velocity and the noise amplitude depending on the mesh size (figure 11). Non-linear, higher-order interpolations are expected to improve the respective mapping accuracy for both methods. For the ICM method, for example, a highly accurate bicubic spline interpolation has been used in a Monte Carlo study of heat conductivity in stochastic boundaries applied to the TEXTOR ergodic divertor [18].

Figure 12 shows a reconstruction of the strongly stochastic layer of the LHD helical divertor by the linear RFLM technique. The field lines are defined on a simple grid of concentric ellipses. A one-cut per field period provides sufficient accuracy in spite of the strong ergodicity. The zoomed details show that high-order resonance islands are reproduced with the same accuracy as the main plasma flux surfaces (see innermost contour).

In a first physics application, the new mapping technique has been used to solve the energy balance equation for an open W7-AS island structure with the EMC3-EIRENE code (figure 13). The grid is defined in the $\phi = 36^{\circ}$ plane and consists of up/down symmetric concentric ellipses. The temperature distribution in the $\phi = 0^{\circ}$ plane preserves the up/down symmetry of the configuration in spite of the asymmetric grid at this toroidal position, as shown in the picture.

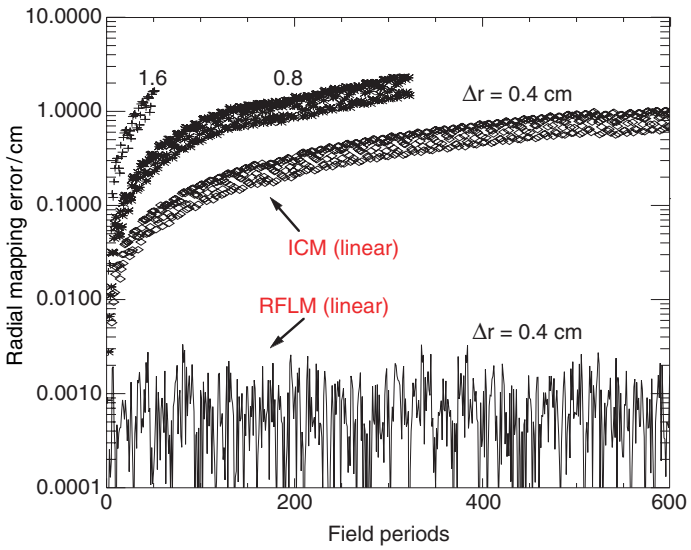

Figure 11. Radial deviations of a mapped field line from its 'exact' position for a W7-AS flux surface from the RFLM and ICM techniques. Starting position $R = 183\,\mathrm{cm}$, $z = 0$ at triangular plane, $\Delta r =$ average mesh width.

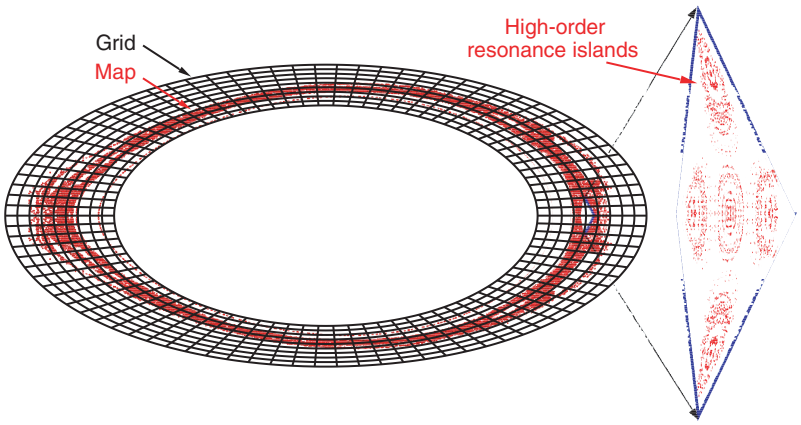

Figure 12. Reconstruction of the strongly stochastic boundary layer of LHD by the RFLM technique. High-order resonances are resolved as accurately as main flux surfaces.

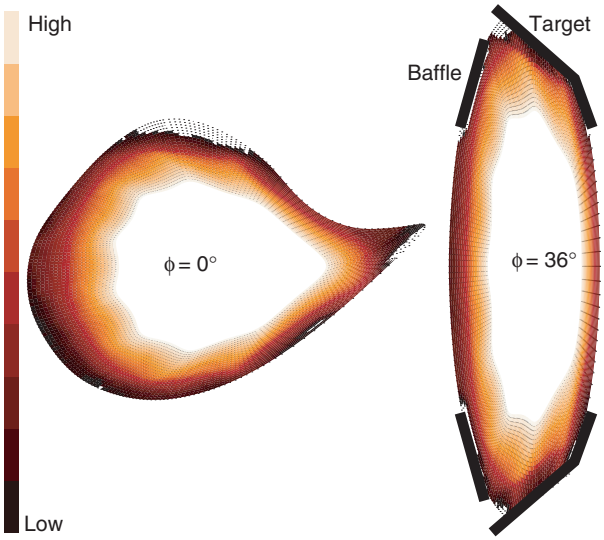

Figure 13. Temperature distribution in the W7-AS island divertor from the solution of the energy balance equation with the RFLM technique.

7. Conclusions

The island divertor concept is emerging as a viable and efficient solution for plasma exhaust and particle control in stellarators. Simple parallel transport models like the two-point model, which describes the standard transport regimes in tokamak divertors, need critical assessment if applied to island divertors mainly because the weight of the parallel transport in the island divertor geometry is substantially reduced in favour of the cross-field transport by the small field-line pitch and plasma-to-target distance. In W7-AS, for example, 3D transport simulations predict a suppression of the high-recycling regime prior to detachment due to parallel momentum losses arising from cross-field particle transport. Specifically, the downstream density increases linearly with the upstream density up to rollover. Furthermore, the upstream

temperature, unlike in the two-point model, drops with increasing upstream density due to cross-field heat transport. These basic effects have been verified recently by the W7-AS divertor experiment. Density rollover appears in the 3D calculations when the ionization front detaches from the target, and a subsequent sharp drop of the downstream temperature and density indicate energy and particle detachment. The W7-AS energy detachment physics can be described by cross-field heat transport and radiation, as shown by both 3D numerical studies and simple 1D models. A condition for stable detachment has been derived from the radial heat transport equation with impurity radiation. For experimentally relevant separatrix densities, the EMC3-EIRENE code predicts a sharp increase of the impurity radiation losses at detachment transition, which has been confirmed by bolometric measurements. This effect is consistent with a thermal instability due the typical form of the impurity cooling rate function.

The presented numerical studies for W7-AS have been carried out on a model configuration with closed magnetic islands. This is an acceptable approach for the effects discussed in this paper, because the field ergodicity is small and the downstream cross-field transport dominates. Strongly ergodic configurations in stellarators and tokamaks, like LHD and TEXTOR-DED, however, cannot be approximated by closed magnetic structures and need an open flux-tube treatment. This problem has been solved by introducing a new highly accurate field-line mapping technique, which provides a very efficient tool to trace arbitrary field lines by simultaneously reducing numerical diffusion of the parallel into the cross-field direction.

References

[1] Kisslinger J, Beidler C D, Harmeyer E, Ran F, Renner H and Wobig H 1994 *21st EPS, Montpellier 1994, Europhys. Conf. Abstracts* **18B** 368
[2] Sardei F *et al* 1997 *J. Nucl. Mat.* **241–243** 135
[3] Grigull P *et al* 1997 *J. Nucl. Mat.* **241–243** 935
[4] Feng Y, Kisslinger J, Sardei F 1999 *26th EPS Conf. (Maastricht)*
[5] Komori A *et al* 1997 *Proc. 16th Int. Conf. on Fusion Energy (Montreal, 1996)* vol 2 (Vienna: IAEA) p 3
[6] Feng Y, Sardei F and Kisslinger J 1999 *J. Nucl. Mat.* **266–269** 812
[7] Reiter D 1984 *Technical Report* Jül-1947, KFA Jülich, Germany
[8] Feng Y, Herre G, Grigull P and Sardei F 1998 *Plasma Phys. Control. Fusion* **40** 371
[9] Feng Y, Sardei F, Kisslinger J, Reiter D and Igitkhanov Y 2001 *28th EPS Conf. (Madeira)*
[10] Rosenbluth M N, Sagdeev R Z, Taylor J B and Zaslavski G M 1966 *Nucl. Fusion* **6** 297
[11] Gadelmeier F *et al* 2001 *28th EPS Conf. (Madeira)*
[12] Post D E 1995 *J. Nucl. Mat.* **220–222** 143
[13] Grigull P *et al* 2001 *Plasma Phys. Control. Fusion* **43** A175
[14] Grigull P *et al* 2002 *12th Int. Toki Conf.* (Toki City, 11–14 December) *J. Plasma Fusion Research* at press
[15] McCormick K *et al* 2002 *Phys. Rev. Lett.* at press
[16] McCormick K, Grigull P, Ehmler H, Feng F, Haas G, Knang J P and W7-A5 team 2001 *28th EPS Conf. (Madeira)*
[17] Tongue B H 1987 *Physica* D **28** 401
[18] Runov A M, Reiter D, Kasilov S V, Heyn M F and Kernblicher W 2001 *Phys. Plasmas* **8** 916